A new supramolecular semi conductor cobalt organometallic complex: Structural study, optical and electrical properties

A. Ben Nasr, Abderrazek Oueslati, Thierry Roisnel, Walid Rekik

A new supramolecular semi conductor cobalt organometallic complex: structural study, optical and electrical properties

BEN NASR Ameni[a], OUESLATI Abderrazek[b], ROISNEL Thierry[c] and REKIK Walid[a*]

[a] Laboratory Physical-Chemistry of Solid state, Chemistry department, Faculty of Sciences of Sfax, University of Sfax, BP 1171, 3000 Sfax, Tunisia.

[b] Laboratory of spectroscopic characterization and optical Materials, Faculty of Sciences, University of Sfax, BP 1171, 3000 Sfax, Tunisia.

[c] Université de Rennes, CNRS, Institut des sciences chimiques de Rennes, UMR6226, F-35042 Rennes, France.

AUTHOR INFORMATION

* Corresponding author, E-mail: walid.rekik@fss.usf.tn

Highlights

- Two different coordination spheres around cobalt cations in a suprmolecular hybrid material.
- The DSC curve reveals the presence of one phase transition which is confirmed by electrical measurements.
- Optical properties confirm the semi-conducting nature of the title complex with an indirect band gap.
- Electric measurements reveal the presence of relaxation phenomenon.

ABSTRACT

Crystals of a novel Cobalt complex $[Co(C_3H_7NO)_6][CoBr_{1.93}Cl_{2.07}]$ were synthesized by a slow evaporation technique at room temperature. Crystal structure, energy dispersive X-ray spectroscopy (EDX), FT-Infrared (IR), thermal behavior, optical analysis, and impedance spectroscopy measurements were provided to characterize this complex. The crystal structure study showed that the cohesion of this complex is assured through N-H…Br/Cl and N-H...O hydrogen bonds giving birth to a 3-D architecture. Infrared spectroscopy is realized to confirm the structural composition and examine the vibrational properties of this complex. The optical absorption spectrum shows that this new complex has an indirect band gap of Eg = 3.71 eV. Differential scanning calorimetry analysis (DSC) showed an endothermic peak around 354 K on heating, which is assigned to a phase transition since no decomposition of the titled compound is evidenced by thermogravimetric analysis (TGA). The temperature dependence of the conductivity (σ_{dc}) and the dielectric properties confirm the presence of this phase transition already observed by thermal analysis. A deep investigation of complex impedance spectra showed that the electrical properties of the material are heavily dependent on frequency and temperature, indicating a relaxation phenomenon and semi-conductor-type behavior.

Keywords: Crystal structure, thermal behavior, optical, complex impedance, relaxation phenomenon.

INTRODUCTION

In the fields of coordination chemistry **[1]**, hybrid organic-inorganic materials specifically, organometallic complexes have emerged as one of the most promising fields of research that has attracted a huge number of scientists. Owing to their unusual structural features **[2-4]** and their unique physico-chemical properties **[5-9]**, these materials have demonstrated exceptional technological applications in various domains including catalysis, biomedicine, magnetism, electrochemical energy storage, and even in sensing devices **[10-13]**.

Since these complexes are composed of metal centers that are linked to organic ligands through coordination links, various properties of both organic and inorganic components can be manifested. In fact, the inorganic clusters demonstrate impressive properties such us magnetic, luminescence, biology, optical, dielectric, and ferroelectric properties **[14-18]**. Whereas, the introduction of organic ligands leads to a better adaptation and functionalization of these materials. As a result, the combination of both components can provide the opportunity to integrate practical properties within a single composite, resulting in a diverse range of multi-functional complexes. As a result, they are a good candidate for photo-active devices such as optoelectronic and photovoltaic, magnets.

Particularly, metal complexes have been recently considered as one of the most promising candidates in terms of their unique structural diversity and properties as well as their fascinating field of applications **[19, 20]**. The literature has pointed to some previously reported works of cobalt complexes containing halide ions such as chloride, bromide ions, or even substitution of both chloride by bromide atoms **[21-24]**. These latter can play an impressive role to understand not only their structural features but also their optical and electrical properties.

In 2005, K. B. Girma et *al.* reported Cobalt(II) complex with the formula [Co-$(CH_2CHC(O)NH_2)_6$][$CoCl_4$]. This compound is stabilized through different types of hydrogen bonding and weak intermolecular interactions, where the amine hydrogen atoms are bonded to a neighboring coordinated oxygen atom and the anion **[21]**. N. M. Kolyadina et *al.* (2013) synthesized a new complex with the formula [Co(L)(H_2O)][$CoCl_4$]. From a structural point of view, the cationic and anionic moieties of this complex are linked through the bridging chlorine atom **[22]**. N. Dege et *al.* recently synthesized and characterized a novel complex, diaquabis(6-chloropyridine-2-carboxylato-N,O)cobalt(II), which exhibits good semi-conducting properties and a band gap energy value of 4.29 eV, and they appears be an interesting candidate for photovoltaic and optoelectronic devices **[23]**. In addition, M. F. Mostafa et *al*. have also synthesis a mixed halide complex with the formula [$(CH_2)_7(NH_3)_2$]$CoCl_2Br_2$. Its crystal structure consists of distorted tetrahedral $[CoCl_2Br_2]^{2-}$ anions and zigzag $[(CH_2)_7(NH_3)_2]^{2+}$ cations linked by intermolecular hydrogen bonds. These latter have demonstrated interesting electric and dielectric properties, which are confirmed by the presence of a relaxation phenomenon and highlight the good ionic conductor of this material **[24]**.

In the present study, we report the synthesis of a novel Cobalt organometallic complex with the formula [$Co(C_3H_7NO)_6$][$CoBr_{1.93}Cl_{2.07}$], a detailed crystallographic study, thermal and spectroscopic analysis. In addition, these investigations are complemented by a deep study of the electrical and optical properties in order to further understand the physical phenomena that govern the behavior of the studied complex.

EXPERIMENTAL DETAILS

Synthesis

Materials

Cobalt(II) chloride hexahydrate ($CoCl_2.6H_2O$), Hydrobromic acid (HBr; 33%), propionamide (C_3H_7NO). All these starting materials were purchased from Sigma–Aldrich and used without further purification.

Preparation of $[Co(PM)_6][CoBr_{1.93}Cl_{2.07}]$

The novel Cobalt complex with the formula $[Co(C_3H_7NO)_6][CoBr_{1.93}Cl_{2.07}]$ was prepared by slow evaporation technique, at room temperature. 2 mmol of propionamide (C_3H_7NO) (hereafter abbreviated PM) and 1 mmol of $CoCl_2 \cdot 6H_2O$ were dissolved together in 10 ml of N,N-diméthylformamide (DMF). Then, 2 mmol of Hydrobromic acid (HBr) were added dropwise to the binary solution. After a few days, blue prism-shaped crystals suitable for X-ray diffraction studies were formed.

Energy dispersive X-ray spectroscopy (EDX) analysis

The elemental analysis was obtained using a Si(Li) detector equipped with an energy dispersive X-ray spectroscopy (EDX).

Spectroscopic measurements

The IR spectrum of the title complex was recorded at room temperature and measured using a Perkin-Elmer BX spectrometer. The sample was dispersed in spectroscopic grade KBr pellets in the wavenumber range of 400–4000 cm^{-1}.

X-ray data collection

The single-crystal X-ray diffraction measurement of this complex was performed at 150K on a APEXII Bruker-AXS diffractometer using Mo-Kα radiation (λMoKα = 0.71073 Å). 7462 reflections were recorded, and among them 5236 checked the condition of intensity $I \geq 2\sigma(I)$. The crystal structure was solved in the monoclinic symmetry with the centrosymmetric space group $P2_1/c$. Co(II) ions were located with Patterson methods using the ShelxT-2018 program **[25]** integrated into the WINGX interface **[26]**.

The nitrogen, carbon, chlorine, and bromine atoms were fixed from successive difference Fourier calculations and refined during the final cycles with anisotropic thermal parameters using the SHELXL-2018 program **[27]**. The positions of the H atoms of the organic molecule are geometrically generated via the HFIX instruction included in SHELXL-2018 with N-H = 0.88 Å and C-H = 0.99 or 0.98 Å. The refinement of the structure ultimately led to the reliability factors R_1 = 0.034 and wR_2 = 0.067. Further, all drawings of the crystal structure were made using the Diamond software package **[28]**.

Crystallographic data and structure refinements are given in **Table 1**. Atomic coordinates and equivalent thermal factors (U_{eq}) or isotropic (U_{iso}) as well as the anisotropic thermal stirring factors are summarized in **Table S1** and **Table S2** respectively.

Table 1. Crystallographic data and structure refinements of $[Co(PM)_6][CoBr_{1.93}Cl_{2.07}]$ complex

Formula	**$[Co(C_3H_7NO)_6][CoBr_{1.93}Cl_{2.07}]$**
Color/Shape	Blue/Prism
Formula weight ($gmol^{-1}$)	784.04
Crystal system	Monoclinic
Space group	$P2_1/c$
Density	1.592
Crystal size (mm)	0.54 × 0.37 × 0.35
Temperature (K)	150(2)
Diffractometer	APEXII Bruker-AXS
a, b, c (Å)	15.4532(11), 11.0869(9), 19.3202(13)
β (°)	98.708(3)
V (Å^3)	3271.9(4)
Z	4
Radiation type	Mo *Kα* (0.71073 Å)
Absorption Correction	multi-scan
θ range for datacollection(°)	$1.3 \leq \theta \leq 27.5$
Measured reflections	21256
Independent reflections	7462
Observed data [I > 2σ (I)]	5236
Index ranges	h = −20→18, k = −8→14, l = −23→24
F(000)	1587
R_{int}	0.043
R[F^2> 2σ(F^2)],wR(F^2),S	0.034, 0.067, 1.007
Δ*ρ*max, Δ*ρ*min(e$Å^{-3}$)	0.55, −0.38

Hirshfeld surface analysis

In order to give more information about the intermolecular interactions already observed within the crystal packing, we have studied the Hirshfeld surfaces (HS) **[29-36].** The 3D Hirshfeld surfaces (HS) and the associated 2D fingerprint (FP) plot calculations were performed using the Crystal Explorer 17.5 program **[37]**. In fact, the 3D Hirshfeld surface is defined by the normalized contact distance (d_{norm}) based on d_e (distance from the point to the nearest nucleus external to the surface), d_i (distance to the nearest nucleus internal to the surface) and the radii of Van Der Waals.

The normalized contact distance (d_{norm}) values were mapped on to the Hirshfeld surface by employing a color gradient varying from blue to red through white was used to quantify the inter-contacts taking place between the atoms within the crystal being studied. The blue color represents longer contacts and a positive d_{norm} value. However, the white color results in contacts exactly equal to the Van Der Waals separation with a d_{norm} value of zero and the red color corresponds to closer contacts and a negative d_{norm} value.

Thermal analysis

In order to study and understand the thermal behavior of the Cobalt(II) complex, thermogravimetric analysis (TGA) was performed by heating 4.65 mg of powdered sample in the temperature range of 300 to 873 K with a ramp rate of 10 $K.min^{-1}$.

Differential scanning calorimetry (DSC) measurements for $[Co(PM)_6][CoBr_{1.93}Cl_{2.07}]$ was carried out using a Perkin-Elmer DSC instrument with heating and cooling rates of 5 $K.min^{-1}$ in the temperature range 300-473 K under nitrogen atmosphere in an aluminium crucible.

Ultraviolet–visible (UV–vis) absorption spectrum

The optical properties of the new Cobalt(II) complex are measured at room temperature using a UV–Vis absorption spectrometer for the spectrum range from 200 to 900 nm.

Electrical measurements

The electrical measurements were carried out by means of two silver electrodes of the configuration Ag/electrolyte/Ag. Furthermore, the polycrystalline material was pressed into 1.2 mm thick pellets with an 8 mm diameter by applying a 3t/cm^2 uniaxial pressure. The electrical transport properties were measured on this pellet in the frequency range of 20 Hz–7 MHz using a 1260 Solartron Impedance Analyzer automatic bridge monitored by a microcomputer. The measurements were taken over the temperature range of 293–423 K. The spectra were fitted to equivalent circuits using the Z-View software.

RESULTS AND DISCUSSION

Energy dispersive X-ray spectroscopy (EDX) analysis

Energy dispersive X-ray spectroscopy (EDX) is an excellent tool for the qualitative identification of the different chemical elements existing in this complex. The chemical purity of the sample was tested by the EDX measurements. Figure S1 (supplementary informations) exhibits the EDX spectrum of the title compound, which reveals the presence of all non-hydrogen chemical elements: Co, Br, Cl, C and N.

Infrared analysis

The IR spectrum revealed by this complex is shown in Figure S2 (supplementary informations). An attempt to assign the major bands is proposed by referring to past work on similar compounds published in the literature **[38, 39]**.

This IR absorption spectrum reveals the presence of two significant bands at 3421 and 3111 cm^{-1}, which can be attributed to the asymetric and symetric stretching modes $\nu_{as}(NH_2)$

and $\nu_s(NH_2)$ of the ligand, respectively. The two close bands at 2962 and 2858 cm^{-1}; correspond to the asymetric and symetric stretching (ν) vibrations of the CH_3 group, respectively. In addition, the symetric stretching modes of the CH_2 group appear at 2807 and 2769 cm^{-1}. The band situated at 1658 cm^{-1} is attributed to the C = O stretching modes in the organic group. Additionally, the $\beta(NH_2)$ bending mode is observed in the infrared spectrum at 1570 cm^{-1}, while the $\beta_{as}(CH_3)$ vibration mode and the $\delta_{as}(CH_3)$ scissoring mode are appeared at 1459 cm^{-1}. The $\beta(CH_2)$, $\beta_s(CH_3)$ and ν(C-N) vibration modes are located at 1410 cm^{-1} and the peak observed at 1376 cm^{-1} is assigned to the $\beta_s(CH_3)$, $\delta_s(CH_3)$ and the $\omega(CH_2)$ wagging mode. Also, the band of low intensity observed at 1084 cm^{-1} is related to the $\rho(CH_3)$, $\rho(CH_2)$ rocking modes and to the $t(CH_2)$ twisting mode. On the other hand, the band noticed at 1006 cm^{-1} corresponds to ν_s(C-C), $\rho(CH_3)$ and $\omega(CH_2)$. At the end, the bands located at 874 cm^{-1} and 813 cm^{-1} are due to the modes $\rho(CH_3)$, $t(CH_2)$, ν_s(C-C) and the π_{Co} out-of-plane bending.

All attributions of the different modes of vibration relating to the title complex are grouped together in **Table S3** (supplementary informations).

Structure description

The studied Cobalt complex, $[Co(PM)_6][CoBr_{1.93}Cl_{2.07}]$, crystallizes in the $P2_1/c$ centrosymmetric space group belonging to monoclinic system with four formula units per cell and the following parameters: *a* = 15.4532(11) Å; *b* = 11.0869(9) Å; *c* = 19.3202(11) Å, β = 98.708(3)° and V = 3271.9(4) $Å^3$.

Figure 1 shows the formula unit extended by symmetry to give a competed coordination sphere around the Co atom. It contains three metal centers of Co(II), twelve PM ligands and four Br/Cl anions. It should be noted that the metal centers Co(1) and Co(2) are located in special positions on the inversion centers (Wyckoff sites (2c) and (2d), respectively), while the third atom Co(3) full general position (Wyckoff site (4e)).

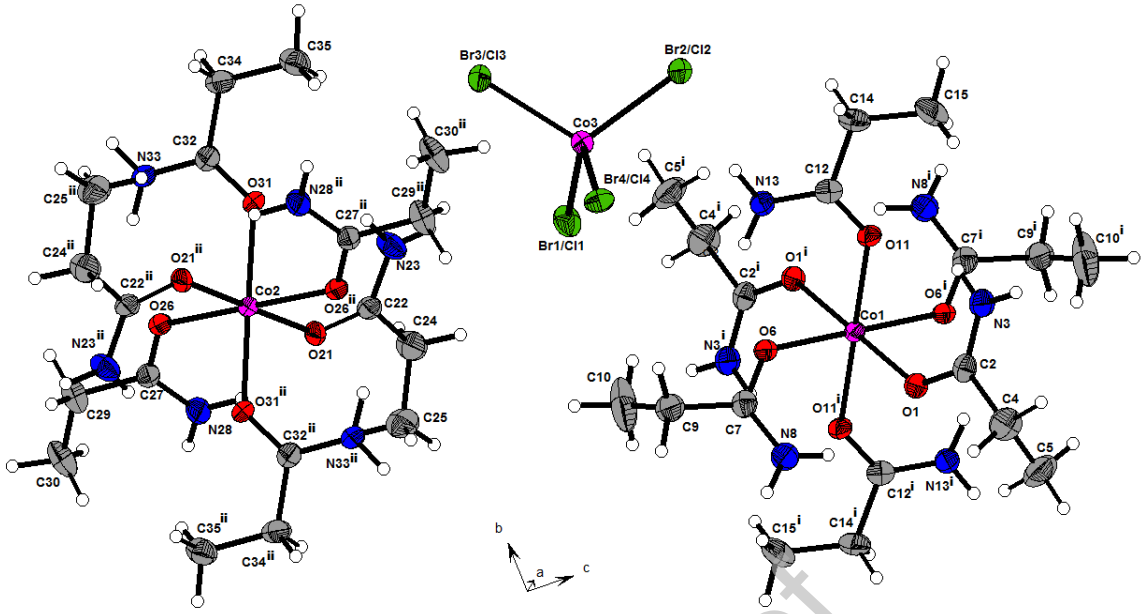

Fig. 1. Representation of the formula unit of $[Co(PM)_6][CoBr_{1.93}Cl_{2.07}]$ extended by symmetry to give complete octahedra around Co(II) cations (symmetry codes: (i) $-x+2, -y+2, -z+1$; (ii) $-x+1, -y, -z+1$)

In the crystal structure, the metallic centers Co(1) and Co(2) adopt an octahedral geometry, where the coordination sphere around Co(1) and Co(2) is formed by six oxygen atoms belonging to six different PM ligands. Further, the values of the Co-O distances located in the equatorial planes vary from 2.0679(17) to 2.0728(17) Å and from 2.0838(17) to 2.0974(17) Å, in the first and second octahedra, respectively, while the Co-O distances of the apical positions are equal to 2.1214(17) and 2.1049(17) Å for Co(1) and Co(2) atoms, respectively. These values are in the same range with those observed in the Co(O-acrylamide)$_4$Cl$_2$ complex where the Co-O bond lengths are 2.0699(15) and 2.1086(13) Å **[21]**.

The *cis*-O-Co-O angles are comprised between [86.25(7)-93.75(7)°] and [85.85(7)-94.15(7)°] for [Co1(PM)$_6$] and [Co2(PM)$_6$] octahedra, respectively **(Table S4**; supplementary informations). We should note that the Co-O distances located in apical positions are longer than the other Co-O distances located in equatorial planes. Thus, confirming that the two

octahedra are elongated in the axial direction. Such a phenomenon reveals the existence of the Jahn-Teller effect. Therefore, the average values of the distortion indices of the different distances for these two octahedra are calculated using the following equation:

$$ID_{(M-L)} = \sum_{i=1}^{i=6} \frac{|ML_i - ML_m|}{6ML_m}$$

The average values of the distortion parameters of the two octahedra in this structure are $ID_{d(metal\text{-}ligand)}Co(1)$ = 0.0018 and $ID_{d(metal\text{-}ligand)}Co(2)$ = 0.0006. For these two octahedra, these low values clearly indicate that the coordination geometry of the metal is a slightly distorted octahedra. It is intersting to note that there are two types of coordination sphere around cobalt atoms in this complex. Indeed the third Co atom in the formula unit is surrounded by only four Br/Cl atoms. For the Co(3) atom, three geometries can be observed: tetrahedron, square plane, or seesaw geometry. To determine the geometry of our cobalt polyhedral, we calculated the τ_4 parameter (τ_4 = 0 for a square plane geometry and τ_4 = 1 for a tetrahedral form) using the following formula:

τ_4 = 360 – (α + β) / 360 - 2θ [40]

With α and β are the two large angles in the polyhedron and θ the angle in a regular tetrahedron, 109.5°.

The calculation of the τ_4 parameter in our cases, considering α = 113.20(2) and β = 111.73(2) leads to τ_4 = 0.96. This result shows that the polyhedron of the Co(3) atom adopt a tetrahedral geometry. The Co-Br/Cl distances are between 2.2907(7) and 2.4084(5) Å and the Br/Cl-Co-Br/Cl angles vary from 104.21(2) to 113.20(2)° **(Table S4)**, which are similar to those found in Co(O-acrylamide)$_4$Cl$_2$ complex (Co-Cl bond lengths are 2.2582(9) and 2.2783(7) Å) **[21]**.

In order to qualify the deformation of these tetrahedra, a calculation of the distortion indices of the distances and the angles was performed according to the method described by Baur **[41]**.

$$ID_{(Co-Br/Cl)} = \sum_{i=1}^{n1=4} \frac{|di - dm|}{n_1 dm} \quad (1)$$

$$ID_{(Br/Cl-Co-Br/Cl)} = \sum_{i=1}^{n2=6} \frac{|ai - am|}{n_2 am} \quad (2)$$

Where, d_m denotes the mean value for distance (Co-Br/Cl) and a_m the mean value for angle (Br/Cl-Co-Br/Cl). These values were 0.0037 and 0.0034, respectively. For the $Co(Br/Cl)_4$ tetrahedra, the distortion indices are low, this confirms that the coordination geometry of the Co(II) metal is a slightly deformed tetrahedron.

The cobalt ions are moderately separated with the shortest inter-metallic Co-Co distance being 6.95(2) Å. Bond distances and angles are comparable to those reported in other similar Co-based hybrid compounds $[Co\{O\text{-}OC\text{-}(NH_2)CHCH_2\}_6][CoCl_4]$ **[21]**, $(PhCH_2NEt_3)_2[CoBr_4]$ **[42]**, $[Co(TPBP)(bpy)_2]$ **[43]**.

The PM ligand is coordinated with the central ions according to the μ1: η1 bridging mode connecting the metal centers through an oxygen atom **(Fig. 1)**. The C-N, O-C and C-C distances vary from 1.314(3) to 1.328(3) Å, from 1.245(3) to 1.262(3) Å and from 1.497(4) Å to 1.525(4) Å, respectively. The N-C-C angles are situated between 116.0(2) and 119.5(3)° **(Table S4)**. The distances and the angles of the PM cation are comparable to the previously reported ones for other similar hybrid compound **[44]**.

On the other hand, the $[Co(Br/Cl)_4]^{2-}$ tetrahedra are stacked in a manner that they form anionic inorganic layers while the organometallic cations $[Co(PM)_6]^{2+}$ form another layers and incorporated between two anionic layers. The structure can be consequently described as

an alternation of inorganic and organometallic layers along the crystallographic *c*-axis **(Fig. 2)**.

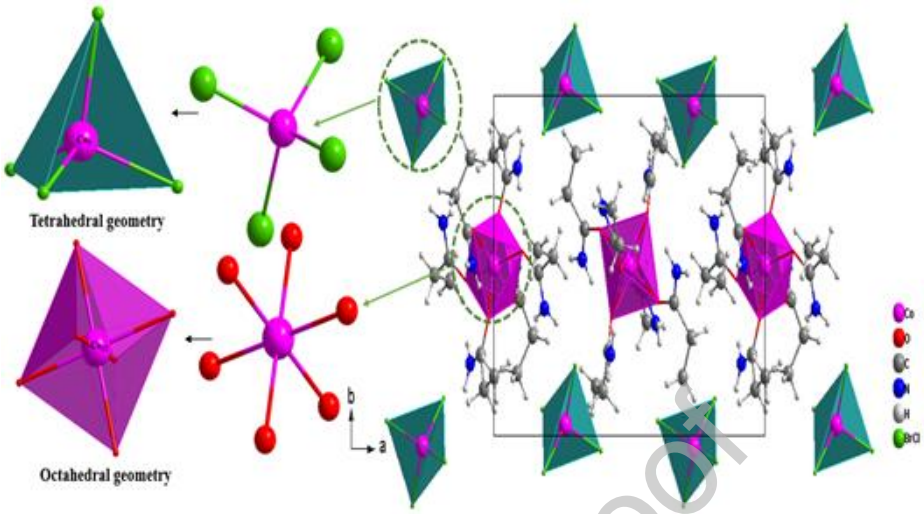

Fig. 2. Packing of $[Co(PM)_6][CoBr_{1.93}Cl_{2.07}]$ along the crystallographic *c*-axis

The cohesion and stability of the crystalline edifice is insured mainly through two types of hydrogen bonds: N-H…Br/Cl and N-H...O **(Fig. 3)**. Indeed, the organic ligands are connected to the Br/Cl anions through hydrogen bonds of the N-H…Br/Cl type, for which the donor-acceptor distances are in the range of 3.201(2) - 3.637(2) Å and the angles range from 131 to 172 °. The distances of N...O interactions fall in the range of 2.864(3) - 3.037(3) Å and the angles range from 139 to 152 °. All these interactions are required for the formation of the pseudo-3D architecture and to stabilize the crystal structure. **Table 2** summarizes the distances and angles that describe hydrogen bonding.

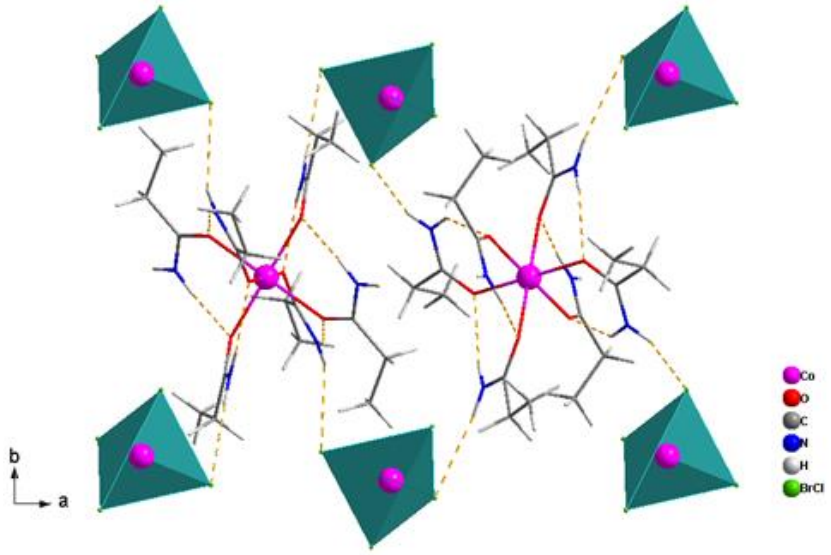

Fig. 3. Packing of $[Co(PM)_6][CoBr_{1.93}Cl_{2.07}]$ showing hydrogen bonds, are represented by dashed lines

Table 2. Hydrogen-bonding geometry of the title complex

D*—H···*A	***D*—H**	**H···*A***	***D*···*A***	***D*—H···*A***
N8—H8*A*···O1	0.88	2.20	2.953 (3)	144
N13—H13*A*···O6	0.88	2.13	2.900 (3)	146
N3—H3*A*···O11	0.88	2.07	2.859 (3)	150
N28—H28*A*···O21^{ii}	0.88	2.06	2.864 (3)	152
N33—H33*A*···O26^{ii}	0.88	2.09	2.894 (3)	151
N23—H23*A*···O31	0.88	2.31	3.037 (3)	139
N3—H3*B*···Br1/Cl1^{iii}	0.88	2.75	3.541 (2)	150
N23—H23*B*···Br1/Cl1^{v}	0.88	2.80	3.637 (2)	161
N13—H13*B*···Br2/Cl2^{iv}	0.88	2.65	3.504 (2)	165
N8—H8*B*···Br3/Cl3	0.88	2.62	3.416 (2)	151
N28—H28*B*···Br4/Cl4	0.88	2.56	3.201 (2)	131
N33—H33*B*···Br4/Cl4^{vi}	0.88	2.54	3.415 (2)	172

Symmetry codes: (ii) −*x*+1, −*y*, −*z*+1; (iii) *x*, −*y*+3/2, *z*+1/2; (iv) *x*, *y*+1, *z*; (v) −*x*+1, *y*−1/2, −*z*+1/2; (vi) −*x*+1, −*y*+1, −*z*+1.

Hirshfeld surface analysis

The corresponding 3D maps of the Hirshfeld surfaces of $[Co1(PM)_6]^+$, $[Co2(PM)_6]^+$, and for the inorganic $[Co3(Br/Cl)_4]^{2-}$ entities mapped over the d_{norm} are shown in Figure S3((a), (b)) (supplementary informations) and 2D fingerprint plots were illustrated in Figure

S4((a), (b)) (supplementary informations), which are used to quantify and visualize the different types of intermolecular interactions.

As reported in Figure S3((a), (b)), it is to be noticed that the red visible spots on the view of the d_{norm} surface of the organic and inorganic sub-lattices are attributed to the hydrogen bonds, Br/Cl…Br/Cl, whereas the Br/Cl…Co/Co…Br/Cl interactions appears in the d_{norm} surface of the organic part. Other white spots are due to the Van der Waals interactions

The 2D fingerprint analysis results of the organic part **(Fig. S4(a))** suggests that the intermolecular H...H contacts have a dominant contribution (66.4%) in the total surface area of cationic part. The second major contribution is Br/Cl...H/H...Br/Cl contact corresponds to 22.3% of the total Hirshfeld surface. At last, the proportions of the other most low interactions of N...H/H…N, C...H/H…C, Br/Cl...Br/Cl, O...H/H…O, O...N/N…O, Co...H/H…Co, C...N/N…C and Br/Cl…Co/Co…Br/Cl are classified in the order of (3.6%), (3%), (1.8%), (1.5%), (0.5%), (0.5%), (0.2%) and (0.2%), respectively.

For the 2D fingerprint of the inorganic part **(Fig. S4(b))**, intermolecular Br/Cl...H/H...Br/Cl contact shows the major contribution with 84.3% in the total Hirshfeld surface area. The Br/Cl...Br/Cl contacts are the second most common interactions, with a relative contribution 12.1% in the total HS of anionic part, whereas the other lowest interactions of Co...H/H...Co and Br/Cl…Co/Co…Br/Cl are 2.4% and 1.2%, respectively.

The relative contributions to the percentage of Hirshfeld surface area for the various intermolecular contacts in this complex are represented in Figure S4((a), (b)). Such results have been confirmed by the X-ray diffraction analysis.

Thermal behavior

TGA and DSC measurements were performed in order to give more information about the thermal stability and to highlight the phase transition presented in this complex. The thermogravimetric curve of the synthesized complex is depicted in Figure 4(a). The examination of this curve shows that the first weight loss is observed between 485 K and 658 K and corresponds to the decomposition of the organic part (observed weight loss = 51.30%; calculated weight loss = 55.92%). The second weight loss observed between 658 and 835K is attributed to the removal of bromide and chloride ions and the formation of cobalt oxide, CoO.

The DSC curve **(Fig. 4(b))** shows an intense peak appearing at 415 K which relates to the melting of the material. This peak is followed by other endothermic peaks observed at 427 K and 437 K, corresponding to the decomposition of the product. We note, moreover, an anomaly at T = 354 K, without any weight loss, which can be explained by a phase transition that can lead to interesting electrical properties. Such a phenomenon is already observed in other cobalt complexes **[14, 23, 45, 46]**.

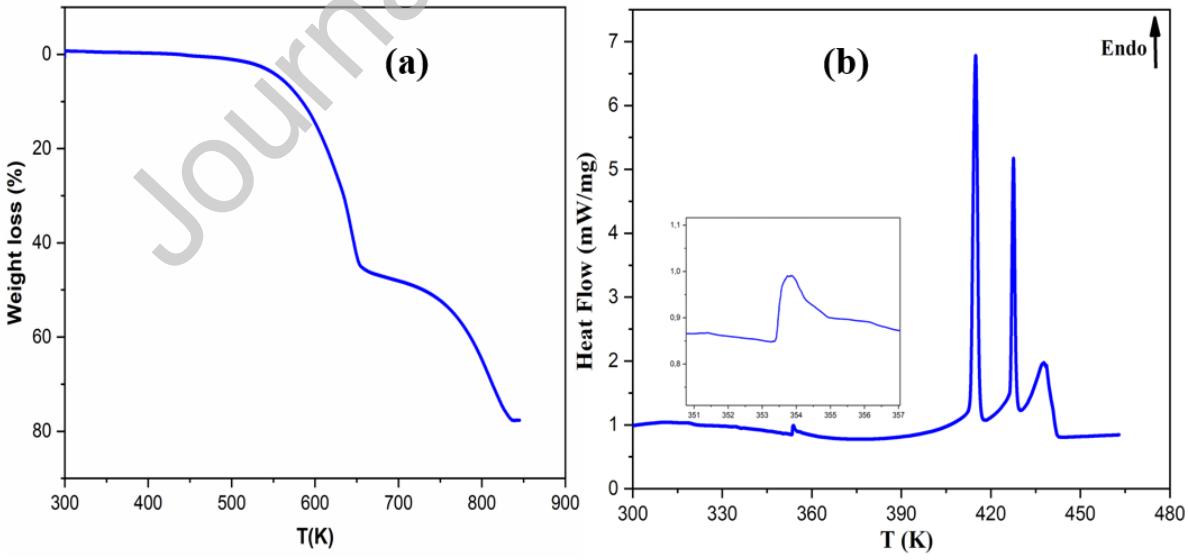

Fig. 4. (a) The TGA analysis curve (b) Differential scanning calorimetry measurements of $[Co(PM)_6][CoBr_{1.93}Cl_{2.07}]$

Optical properties of $[Co(PM)_6][CoBr_{1.93}Cl_{2.07}]$

Figure 5 displays the UV–Visible absorption spectrum of the title complex at room temperature in the 200-900 nm range. As noted, this spectrum shows one intense absorption band at 303 nm and a weak intensity band observed at 456 nm. The latter are attributed to an electronic charge transfer from ligand to metal, usually named as LMCT: transition from the 3p/4p orbital of Cl/Br or the 2p orbital of the oxygen atoms pertaining to the PM organic ligand to the 3d orbital of Co(II). In addition, the bands centered at 537 nm, 631 nm, 663 nm, 688 nm and 722 nm are assigned to the d-d transitions of the metal centers (Co^{2+} ion). The attribution of the different absorption bands is similar to that obtained for other cobalt (II) chloride **[47, 48]** or cobalt (II) bromide **[49]** compounds found in the literature.

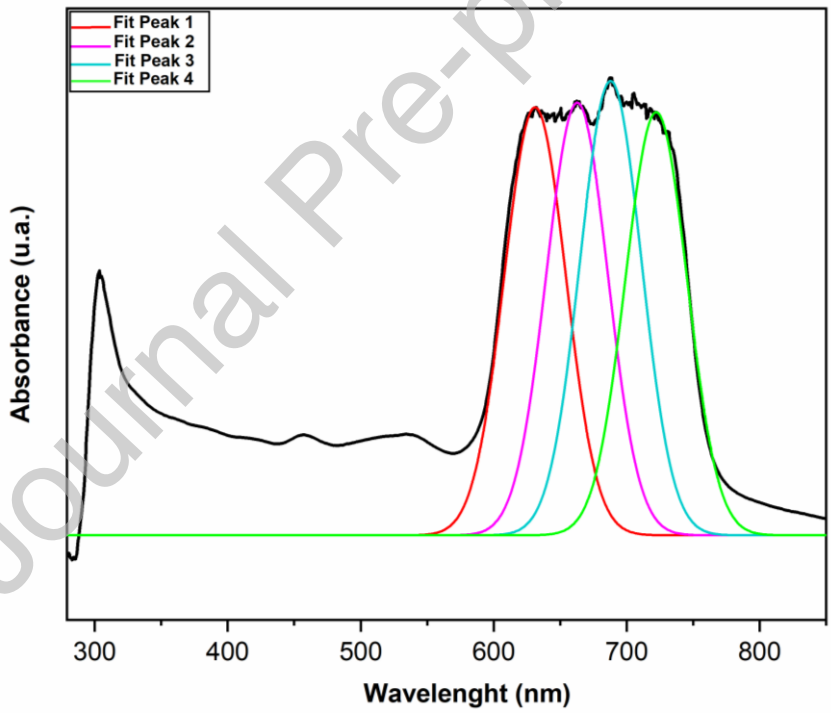

Fig. 5. UV–Visible Absorption Spectra for the title complex

The optical absorption coefficient (α) and the incident photon energy (hυ) are used to determine the optical band gap value using the classical Tauc's relation for direct and indirect band transitions **[50, 51]**:

$$(\alpha h\nu) = (A(h\nu - Eg)^n)$$

Where A is a constant, Eg is the band gap energy, α is the optical absorption coefficient, and n is a constant which determines the type of optical transitions. For direct transition (n = ½), the direct gap energy is noted E_g^d and for indirect transition (n = 2), the indirect gap energy is noted E_g^{in}. A plots of $(\alpha h\upsilon)^2$ and $(\alpha h\nu)^{1/2}$ versus hυ for the new Cobalt complex are illustrated in Figure 6((a), (b)).

On the other hand, the values of the direct and indirect gap energies in this complex are obtained by extrapolating the linear part of the curve with the X-axis. The direct and indirect gap energy values are in the order of 3.54 and 3.71 eV, respectively.

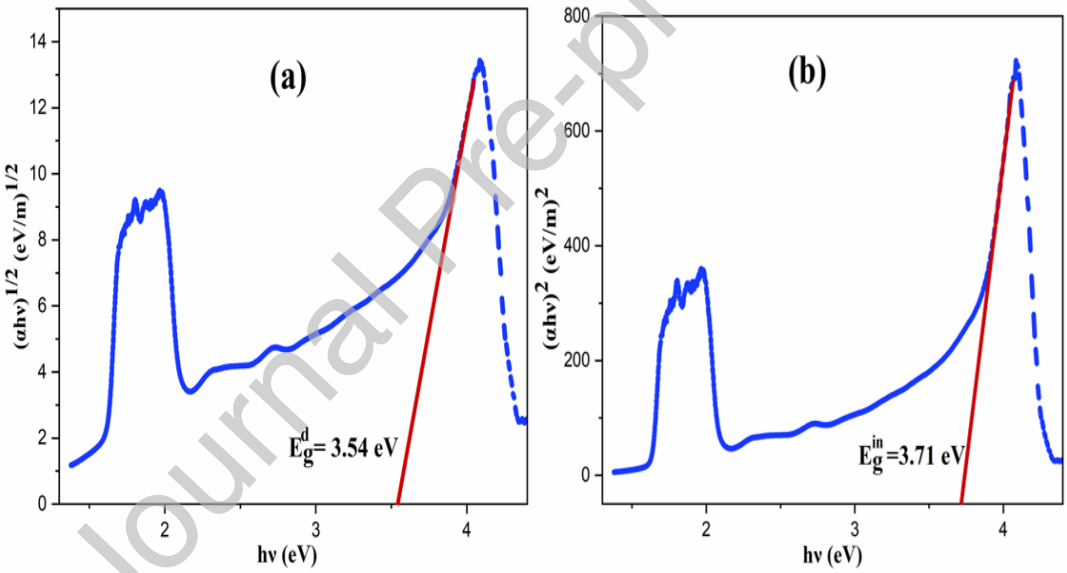

Fig. 6. Variations of (a) $(\alpha h\nu)^{1/2}$ versus hν, (b) $(\alpha h\nu)^2$ versus hν at room temperature for $[Co(PM)_6][CoBr_{1.93}Cl_{2.07}]$

The curve of Ln (αhν) versus Ln (hν - Eg) allows us to determine the value of n, which is the inverse of the slope of the straight line deduced from Figure 7. This value of n almost equals 2, which confirms that the gap transition is of the indirect type.

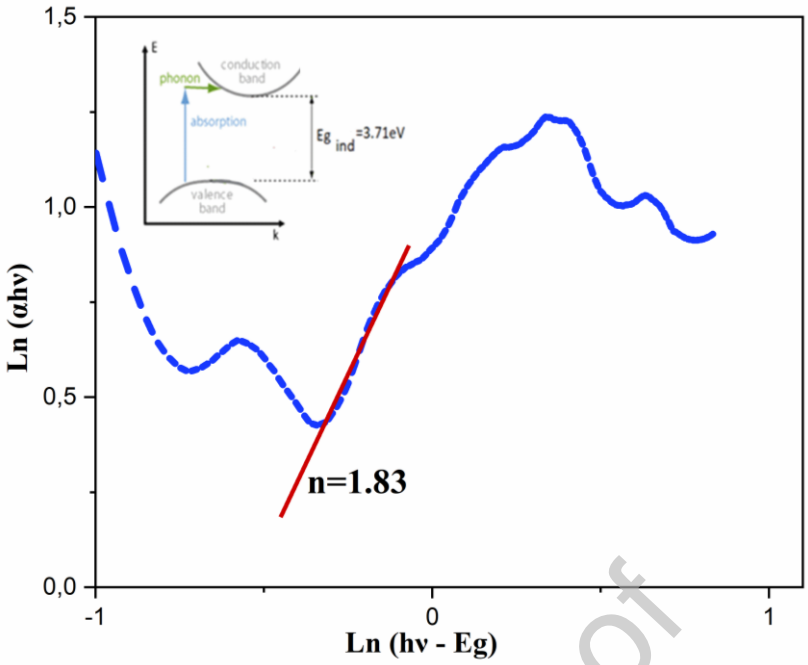

Fig. 7. Variations of (αhν) versus Ln (hν - Eg) and the Energy diagram of $[Co(PM)_6][CoBr_{1.93}Cl_{2.07}]$ complex

Therefore, this interest value can classify this complex among the semiconductor which is required for applications in the fields of photovoltaics and optoelectronics. The estimated Eg equal to 3.71 eV for the title complex is comparable to the calculated values of the band gaps found in the other compounds $[(CH_3)_2NH_2]_2CoCl_4$ (3.84 eV) **[47]**, $[(CH_3)_3N(CH_2)_2Br]_2[CoBr_4]$ (3.7 eV) **[52]**, $[N(CH_3)_4]_2CoCl_4$ (4.59 eV) **[53]**, as well as $[C_8H_{10}NO]_2CoCl_4$ (2.98 eV) **[54]**.

Electrical properties

Impedance analysis and equivalent circuit

In order to gain further insight about the phase transition already present in the DSC measurements and to confirm the semi-conducting nature of the title material, we have performed the electric measurements. For that, Figure 8 depicts the variation of the Nyquist plots (-Z" versus Z') of the title compound from 293 to 423 K. In the temperature range previously explored, the Nyquist plots consist of decentred semi-circles, with the centre located below the Z' axis, which indicates that the Cole–Cole formalism is appropriate to

study this relaxation phenomenon **[55]**. Two semi-circles are observed in the patterns. Thus, the lower frequency dispersion corresponds to the grain boundary (Rjg) and the higher one to the grain interior (Rg). To simulate our sample by an equivalent circuit that accounts for these experimental data, we have used the software Z-View.

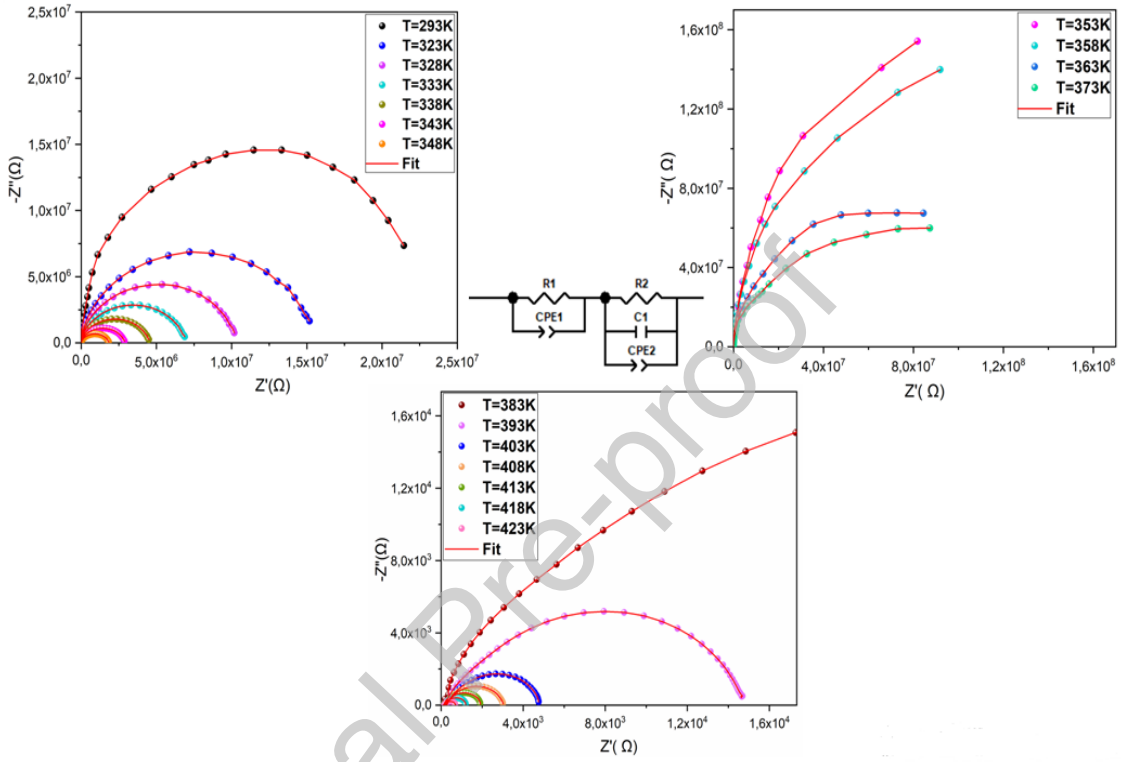

Fig. 8. Complex impedance and equivalent circuit of $[Co(PM)_6][CoBr_{1.93}Cl_{2.07}]$ complex shown for different temperatures

The best fit was obtained by using an equivalent circuit composed of two cells connected in series, the first one being formed by resistance R1 parallel to a fractal capacity CPE1 and the second one being formed of a parallel combination of three elements: resistance R2, capacity C1 and fractal capacity constant phase element CPE2. Note that the fractal capacitance Z_{CPE} impedance is represented by the following equation:

$$Z_{CPE} = \frac{1}{Q_0(j\omega)^{\propto}}$$

Where Q is the capacitance value of the CPE element and α represents the fractal exponent.

The reel and the imaginary part of the complex impedance ((Z') and (Z")) were calculated according to the following equations:

$$Z' = \frac{R_1\left(1+R_1Q_1\omega^{\alpha_1}\cos\left(\alpha_1\pi/2\right)\right)}{\left(1+R_1Q_1\omega^{\alpha_1}\cos\left(\alpha_1\pi/2\right)\right)^2+\left(R_1Q_1\omega^{\alpha_1}\sin\left(\alpha_1\pi/2\right)\right)^2}+\frac{R_2^{-1}+Q_2\omega^{\alpha_2}\cos\left(\alpha_2\pi/2\right)}{(R_2^{-1}+Q_2\omega^{\alpha_2}\cos\left(\alpha_2\pi/2\right))^2+(C\omega^{\alpha_2}\sin\left(\alpha_2\pi/2\right))^2} \quad (1)$$

$$-Z'' = \frac{R_1^2Q_1\omega^{\alpha_1}\sin\left(\alpha_1\pi/2\right)}{\left(1+R_1Q_1\omega^{\alpha_1}\cos\left(\alpha_1\pi/2\right)\right)^2+\left(R_1Q_1\omega^{\alpha_1}\sin\left(\alpha_1\pi/2\right)\right)^2}+\frac{C+Q_2\omega^{\alpha_2}\sin\left(\alpha_2\pi/2\right)}{(R_2^{-1}+Q_2\omega^{\alpha_2}\cos\left(\alpha_2\pi/2\right))^2+(C\omega^{\alpha^2}\sin\left(\alpha_2\pi/2\right))^2} \quad (2)$$

Figure 9(a) shows the imaginary part of the impedance, Z', as a function of frequency at different temperatures. It is observed that at a lower frequency range, the variation of Z' (grain resistance) decreases with rising temperature. As a result, an increase in ac conductivity with increasing frequency is possible. The merge of real part of impedance in the higher-frequency domain suggests a possible release of space charge and a consequent lowering of the barrier properties in the materials **[56]**.

Figure 9(b) represents the variation of the imaginary part Z" according to frequency at different temperatures. These curves display a peak at a specific frequency known as the relaxation frequency (ω_{max}), such that $\omega_{max}\tau = 1$, (where τ is called the relaxation time). The relaxation frequency is not the same for all peaks. Such behavior reflects the non-Debye type of relaxation in the system **[57]**. Also, the widening of peaks and the move of (Z''_{max}) at higher temperatures confirm the presence of relaxation phenomena in the system as well as that there is a spread of relaxation time **[58]**.

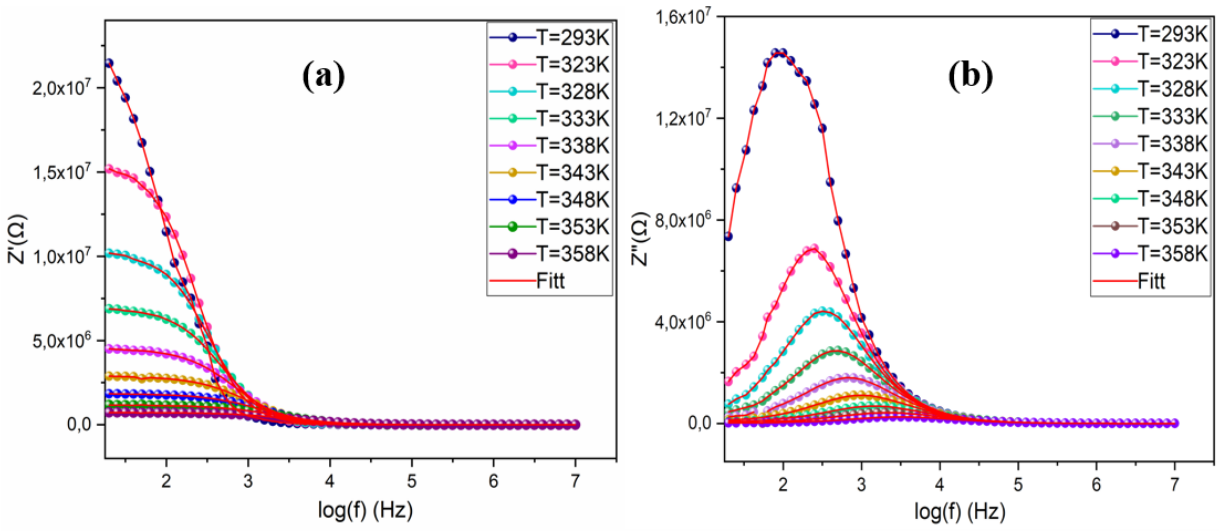

Fig. 9. Frequency variation of (a) Real part Z' and (b) imaginary part Z" of the impedance at different temperatures for $[Co(PM)_6][CoBr_{1.93}Cl_{2.07}]$

Plots detailed in **Figures 8, 9(a) and 9(b)** show a good coincidence between experimental and simulated data indicating that the suggested equivalent circuit describes accurately the electrical properties of the complex.

Relying on the bulk resistance R_1 values and the sample dimensions, the grain electrical conductivity (σ_{dc}), can be calculated at each temperature using the following relationship:

$$\sigma(dc) = \frac{e}{R * S}$$

Where, e and S depict the thickness and the area of the pellets, respectively.

Figure 10 shows the thermal evolution of the conductivity of the grains, (Ln ($\sigma_{dc}T$)) versus 1000/T. The conductivity of the grain increases within creasing temperature, indicating that the electrical conduction in the sample is thermally activated and follows the Arrhenius-type behavior.

$$\sigma_{dc}T = \sigma_0 \exp(-E_a/k_BT)$$

Where, σ_0 represents the pre-exponential factor, E_a is the activation energy for conduction, and k_B is the Boltzmann constant.

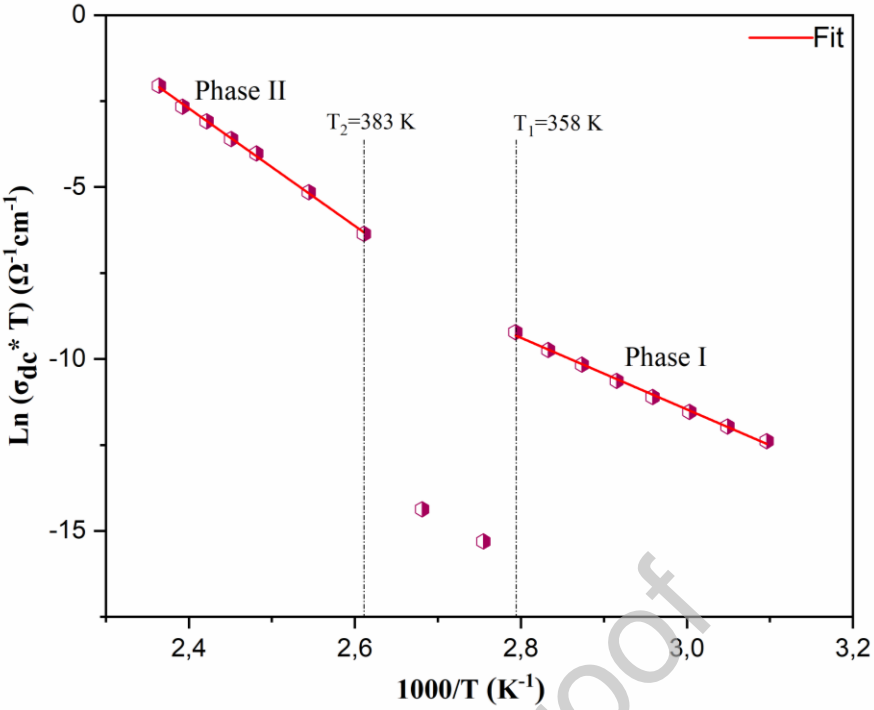

Fig. 10. Variation of (Ln (σ_{dc}T)) versus 1000/T of the [Co(PM)$_6$][CoBr$_{1.93}$Cl$_{2.07}$] complex

Two phases were identified with a change in the curve slope towards T = 358 K, which confirms the phase transition detected by DSC differential thermal analysis at T = 354 K. From the linear fitting, the phase I (T < 358 K) was characterized by a growing conductivity with an activation energy ΔE_I = 0.89 eV. Furthermore, the phase II (T > 383 K) was characterized by an increasing conductivity as the temperature increased, with an activation energy equal to ΔE_{II} = 1.48 eV. These results allow us to classify this material as a good semi-conductor **[52]**.

Complex modulus analysis

The complex modulus formalism is particularly used to determine the conductivity relaxation, the jump frequencies, and also electrode polarization. The complex electrical modulus M* is defined by the inverse of the complex permittivity **[59, 60]**, according to the following equation:

$$M^* = 1/\varepsilon^* = i\omega C_0 Z^* = M'+jM'' = M_\infty \left[1 - \int_0^\infty e^{-iwt}\left(-\frac{d\Phi(t)}{dt}\right)dt\right]$$

Where, M' and M'' represent the real and imaginary parts of the complex modulus M* and C_0 is the vacuum capacitance of the cell and $\Phi(t)$ means the stretched exponential function of a material.

In order to verify the contribution of these different phenomena, we investigated the variation of the real part M' of the complex modulus versus (log (f)), which is shown in Figure S5 (supplementary informations) at different temperatures. Indeed, we notice that at low frequency, this curve displays a very low value of M' which confirms that the electrode effects are negligible. At high frequencies, the real part M' tends towards a constant value ($M'_\infty = 1/\varepsilon'_\infty$) which may confirm the presence of a relaxation process in this studied sample.

Figure S6 (supplementary informations) shows the 3D presentation of the imaginary part of modulus normalized (M''/M''_{max}) according to the frequency for different temperatures. These curves appear as well-defined asymmetric relaxation peaks in which the maxima shift towards higher frequencies through increasing temperature. Such behavior reflects a transition from short distances to long distances mobility of charge carriers **[61]**. In fact, at low frequency region, the ions are mobile over long-distances, while at high frequencies the ions are more confined to their potential wells, being mobile on short-distances. We note that each maximum of M''_{max} corresponds to a characteristic relaxation frequency $fp(fp = \frac{1}{2\pi\tau max})$, where τmax is the most probable relaxation time **[62]**.

In Figure S7 (supplementary informations), the evolution of log (fp) according to the inverse of temperature is shown. We note the relaxation frequency log (fp) is presented by two phases with a discontinuity at 358 and 383 K. These results absolutely confirm the phase transition already observed in DSC analysis and conductivity measurements.

Dielectric studies

The study of dielectric relaxation is a high source of precious information about the

mechanisms of conduction, the origin of the dielectric for different temperatures. The values of the real and imaginary permittivity were calculated from the following equations **[63]**:

$$\varepsilon^* = \varepsilon' + i\varepsilon''$$

$$\varepsilon' = \frac{-Z''}{\omega C_0 (Z'^2 + Z''^2)}$$

$$\varepsilon'' = \frac{-Z'}{\omega C_0 (Z'^2 + Z''^2)}$$

The temperature dependence of the real and imaginary parts (ε'_r and ε''_r) of the dielectric permittivity for the $[Co(PM)_6][CoBr_{1.93}Cl_{2.07}]$ complex at selected frequencies is reported in Figure 11 ((a), (b)), respectively. It is observed that both ε′ and ε″ exhibit similar behavior. From those figures, at temperatures lower than 358 K, that the variations of the ε' and ε'' are almost constants. This behavior indicates the low thermal energy of the charge carriers, which seem unable to peruse the electric field direction **[64]**. This result may be due to an increase of the disorder in the compound leading to a weakening in the crystal interactions **[65, 66]**. As the temperature increases, beyond 358 K, the bound charge carriers get a gradually an amount of thermal excitation energy to be able to respond to the change in the external field more easily and the dipoles can rotate freely. This in turn enhances their contribution to the polarization, leading to an increase of the real and imaginary parts of the dielectric constant **[67]**.

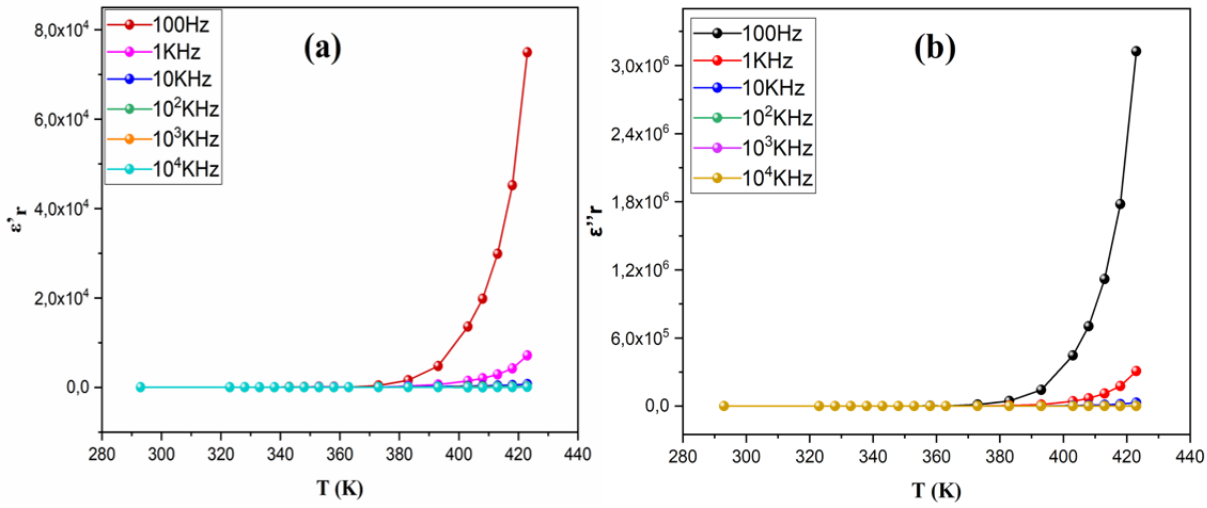

Fig. 11. Temperature dependence of (a) ε'$_r$ and (b) ε''$_r$ for [Co(PM)$_6$][CoBr$_{1.93}$Cl$_{2.07}$] complex at various frequencies

CONCLUSION

In summary, the preparation and characterization of a novel Cobalt complex with the formula [Co(PM)$_6$][CoBr$_{1.93}$Cl$_{2.07}$] was reported. Crystal structure study revealed that this complex belongs to the monoclinic symmetry with the P2$_1$/c space group. Its crystal structure consists of two different coordination spheres around the cobalt atoms. Further, the crystal packing is stabilized by the formation of N-H…Br/Cl and N-H...O hydrogen bonds, giving birth to a 3-D architecture. The optical properties confirmed that the title compound is a semi-conductor with band gap energy of 3.71 eV. The thermal study indicated the presence of one phase transition at T = 354 K that was subsequently confirmed by the electrical and dielectric analyses. Besides, the impedance complex analysis allowed us to determine the electrical equivalent circuit. Electric and dielectric measurements show that this complex is a good semi-conductor. Based on these results, we totally believe that our research work appears to be a promising route to pursue novel semi-conducting compounds and can be a good candidate for specific applications in batteries, electrolytes, and electro-optical devices.

SUPPLEMENTARY MATERIALS

Supplementary crystallographic data for this article in CIF format are available as electronic supplementary publication from Cambridge Crystallographic Data Centre (CCDC 2150505). This data can be obtained free of charge via https://www.ccdc.cam.ac.uk/community/deposita structure/CSD Communications/, or from the Cambridge Crystallographic Data Centre, 12 Union Road, Cambridge CB2 1EZ, UK (Fax: (international): +441223/336033; e-mail: deposit @ ccdc.cam.ac.uk).

conflict of interest

None

Author statement

Ameni Ben Nasr: chemical preparation and writing

Abderrazek Oueslati: electrical measurements

Thierry Roisnel: single crystal X-ray diffraction

Walid Rekik: Validation and supervising

REFERENCES

[1] X.Y. Li, L. Chen, L. Gao, Y. Zhang, S.F. Akogun, W.K. Dong, Syntheses, crystal structures and catalytic activities of two solvent-induced homotrinuclear Co(II) complexes with a naphthalenediol-based bis(Salamo)-type tetraoxime ligand, RSC Adv. 7 (2017) 35905–35916. https://doi.org/10.1039/c7ra06796h.

[2] S. Kansız, A. Tolan, M. Azam, N. Dege, M. Alam, Y. Sert, S. I. Al-Resayes, H. İçbudak, Acesulfame based Co(II) complex: Synthesis, structural investigations, solvatochromism, Hirshfeld surface analysis and molecular docking studies, Polyhedron. 218 (2022) 115762. https://doi.org/10.1016/j.poly.2022.115762.

[3] X.F. Ma, H.L. Wang, Z.H. Zhu, H.H. Zou, B. Liu, Z. Wang, Z.W. Ouyang, F.P. Liang, Solvent-Induced Structural Diversity and Magnetic Research of Two Cobalt(II) Complexes, ACS Omega. 4 (2019) 20905–20910. https://doi.org/10.1021/acsomega.9b01781.

[4] M. Azam, P. K. Sahoo, R. K. Mohapatra, M. Kumar, A. Ansari, I. S. Moon, A. Chutia, S. I. Al-Resayes, S. K. Biswal, Structural investigations, Hirsfeld surface analyses, and molecular docking studies of a phenoxo-bridged binuclear Zinc(II) complex, J. Mol. Struct. 1251 (2022) 132039. https://doi.org/10.1016/j.molstruc.2021.132039.

[5] C. Nde, A. N. Nana, I. N. Kamga, M. Azam, F. Capet, M. Foulon, J. Nenwa, A new bis(oxalato)ferrate(III) hybrid salt associated with guanidinium cations: Synthesis, crystal structure, magnetic properties and Hirshfeld surface analysis, J. Mol. Struct. 1263 (2022) 133145. https://doi.org/10.1016/j.molstruc.2022.133145.

[6] D. Abid, I. Dhouib, P. Guionneau, S. Pechev, I. Chaabane, N. Daro, Z. Elaoud, Proton conduction study of a new selenate-based hybrid compound, J. Alloys Compd. 824 (2020) 153826. https://doi.org/10.1016/j.jallcom.2020.153826.

[7] H. Ltaief, A. Mahroug, M. Belhouchet, Crystal structure, Hirshfeld surface analysis and physicochemical studies of a new copper coordination polymer with 3,3'-diaminodiphenylsulfone as ligand, J. Mol. Struct. 1245 (2021) 131236. https://doi.org/10.1016/j.molstruc.2021.131236.

[8] A. Tesmar, M. Witwicki, D. Wyrzykowski, A. Sikorski, D. Jacewicz, J. Drzeżdżon, L. Chmurzyński, Structure and characterization of physicochemical and magnetic properties of new complex containing monobridged oxygen copper(II) dinuclear cation, Polyhedron. 127 (2017) 144–152. https://doi.org/10.1016/j.poly.2017.02.003.

[10] N. Amiri, M. Guergueb, M.S. Al-Fakeh, M. Bourguiba, H. Nasri, A new cobalt(II): Meso -porphyrin: Synthesis, characterization, electric properties and application in the catalytic degradation of dyes, RSC Adv. 10 (2020) 44920–44932. https://doi.org/10.1039/d0ra08786f.

[11] J.F. Longevial, S. Clément, J.A. Wytko, R. Ruppert, J. Weiss, S. Richeter, Peripherally Metalated Porphyrins with Applications in Catalysis, Molecular Electronics and Biomedicine, Chem. - A Eur. J. 24 (2018) 15442–15460. https://doi.org/10.1002/chem.201801211.

[12] B. Brachňaková, S. Matejová, J. Moncol, R. Herchel, J. Pavlik, E. Moreno-Pineda, M. Ruben, I. Šalitroš, Stereochemistry of coordination polyhedra: Vs. single ion magnetism in penta- And hexacoordinated Co(II) complexes with tridentate rigid ligands, Dalt. Trans. 49 (2020) 1249–1264. https://doi.org/10.1039/c9dt04592a.

[13] S. Li, J. Lin, W. Xiong, X. Guo, D. Wu, Q. Zhang, Q.L. Zhu, L. Zhang, Design principles and direct applications of cobalt-based metal-organic frameworks for electrochemical energy storage, Coord. Chem. Rev. 438 (2021) 213872. https://doi.org/10.1016/j.ccr.2021.213872.

[14] K. Hchicha, M. Korb, A. Kliuikov, E. Čižmár, H. Naïli, A cobalt (II)-based semiconductor complex with two-channel slow magnetic relaxation, J. Magn. Magn. Mater. 536 (2021). https://doi.org/10.1016/j.jmmm.2021.168140.

[15] D. Zhao, X.H. Liu, Y. Zhao, P. Wang, Y. Liu, M. Azam, S.I. Al-Resayes, Y. Lu, W.Y. Sun, Luminescent Cd(II)-organic frameworks with chelating NH2 sites for selective detection

of Fe(III) and antibiotics, J. Mater. Chem. A. 5 (2017) 15797–15807. https://doi.org/10.1039/c7ta03849f.

[16] Zhi-Qiang Liu, Yue Zhao, Xiu-Du Zhang, Yan-Shang Kang, Qing-Yi Lu, Mohammad Azam, Saud I Al-Resayes, Wei-Yin Sun, Metal–organic frameworks with 1,4-di(1*H*-imidazol-4-yl)benzene and varied carboxylate ligands for selectively sensing Fe(III) ions and ketone molecules, Dalton Trans. 46 (2017) 13943-13951. https://doi.org/10.1039/C7DT02981K.

[17] S. Dgachi, F. Rahmouni, A. Soran, M. Saoudi, G. Nemes, H. Naïli, A mononuclear Co(II) complex: Crystal structure, thermal behavior, optical properties and biological activities, J. Mol. Struct. 1244 (2021) 130996. https://doi.org/10.1016/j.molstruc.2021.130996.

[18] N. Amiri, M. Bourguiba, M. Guergueb, S. Chevreux, H. Nasri, Synthesis, molecular structure, spectroscopic characterization and dielectric properties of new cobalt(II) meso-tetraphenylporphyrin-based coordination complex, Inorg. Chem. Commun. 118 (2020) 107995. https://doi.org/10.1016/j.inoche.2020.107995.

[19] M. Azam, S. I. Al-Resayes, A. Trzesowska-Kruszynska, R. Kruszynski, Synthesis, characterization and X-ray crystal structure of a mononuclear ampyrone based zinc complex, J. Mol. Struct. 1259 (2022) 132727. https://doi.org/10.1016/j.molstruc.2022.132727.

[20] M. Azam, G. Velmurugan, A. Trzesowska-Kruszynska, S. I. Al-Resayes, R. Kruszynski, P. Venuvanalingam, A bowl-shaped phenoxido-bridged binuclear zinc complex: Experimental and theoretical studies, Inorganica Chim. Acta. 534 (2022) 120807. https://doi.org/10.1016/j.ica.2022.120807.

[21] K.B. Girma, V. Lorenz, S. Blaurock, F.T. Edelmann, Coordination chemistry of acrylamide 1. Cobalt(II) chloride complexes with acrylamide - Synthesis and crystal

structures, Zeitschrift Fur Anorg. Und Allg. Chemie. 631 (2005) 1419–1422. https://doi.org/10.1002/zaac.200500027.

[22] N.M. Kolyadina, V.I. Sokol, V.B. Kvartalov, V. V. Davydov, E.A. Fomicheva, A.T. Soldatenkov, V.S. Sergienko, Synthesis of a new aza-14-crown-4 with di(α-pyridyl)-substituted bispidine subunit and the crystal structure of its complex with $CoCl_2$, Russ. J. Inorg. Chem. 58 (2013) 671–677. https://doi.org/10.1134/S0036023613060156.

[23] N. Dege, Ö. Tamer, M. Yaman, A. Başoğlu, D. Avcı, Y. Atalay, Crystallographic, spectroscopic, thermal, optical investigations and density functional theory calculations for novel Co(II) and Mn(II) complexes, Appl. Phys. A Mater. Sci. Process. 127 (2021) 1–17. https://doi.org/10.1007/s00339-020-04267-x.

[24] M.F. Mostafa, S. Abd-Elal, A.K. Tammam, Crystal structure, thermal, electric and magnetic study of $[(CH_2)_7(NH_3)_2]CoCl_2Br_2$, Indian J. Phys. 88 (2014) 49–57. https://doi.org/10.1007/s12648-013-0371-8.

[25] G.M. Sheldrick, SHELXT - Integrated space-group and crystal-structure determination, Acta Crystallogr. Sect. A Found. Crystallogr. 71 (2015) 3–8. https://doi.org/10.1107/S2053273314026370.

[26] L.J. Farrugia, WinGX suite for small-molecule single-crystal crystallography, J. Appl. Crystallogr. 32 (1999) 837–838. https://doi.org/10.1107/S0021889899006020.

[27] G.M. Sheldrick, Crystal structure refinement with SHELXL, Acta Crystallogr. Sect. C Struct. Chem. 71 (2015) 3–8. https://doi.org/10.1107/S2053229614024218.

[28] W.T. Pennington, DIAMOND – Visual Crystal Structure Information System , J. Appl. Crystallogr. 32 (1999) 1028–1029. https://doi.org/10.1107/s0021889899011486.

[29] H. Raza, I. Yildiz, F. Yasmeen, K.S. Munawar, M. Ashfaq, M. Abbas, M. Ahmed, H. A. Younus, S. Zhang, N. Ahmad, Journal of Colloid and Interface Science Synthesis of a 2D copper (II)-carboxylate framework having ultrafast adsorption of organic dyes, J. Colloid Interface Sci. 602 (2021) 43–54. https://doi.org/10.1016/j.jcis.2021.05.169.

[30] M. Ashfaq, M. N. Tahir, K. S. Munawar, R. Behjatmanesh-Ardakani, H. Kargar, Single crystal exploration, supramolecular behaviour, Hirshfeld surface analysis, linear and non-linear theoretical optical properties of Schiff bases derived from Benzene sulfonamides, J. Mol. Struct. 1261 (2022) 132952. https://doi.org/10.1016/j.molstruc.2022.132952.

[31] H. Kargar, M. Ashfaq, M. Fallah-Mehrjardi, R. Behjatmanesh-Ardakani, K. S. Munawar, M. N. Tahir, Synthesis, crystal structure, spectral characterization, theoretical and computational studies of Ni(II), Cu(II) and Zn(II) complexes incorporating Schiff base ligand derived from 4-(diethylamino)salicylaldehyde, Inorganica Chim. Acta. 536 (2022) 120878. https://doi.org/10.1016/j.ica.2022.120878.

[32] M. Ashfaq, A. Ali, M. N. Tahir, A. Kuznetsov, K. S. Munawar, S. Muhammad, Synthesis, single-crystal exploration, hirshfeld surface analysis, and DFT investigation of the thiosemicarbazones, J. Mol. Struct. 1262 (2022) 133088. https://doi.org/10.1016/j.molstruc.2022.133088.

[33] M. Haroon, T. Akhtar, M. Yousuf, M.N. Tahir, L. Rasheed, S.S. Zahra, I. ul Haq, M. Ashfaq, Synthesis, crystal structure, Hirshfeld surface investigation and comparative DFT studies of ethyl 2-[2-(2-nitrobenzylidene)hydrazinyl]thiazole-4-carboxylate, BMC Chem. 16 (2022) 1–17. https://doi.org/10.1186/s13065-022-00805-1.

[34] H. Kargar, M. Ashfaq, M. Fallah-Mehrjardi, R. Behjatmanesh-Ardakani, K. S. Munawar, M. N. Tahir, Theoretical studies, Hirshfeld surface analysis, and crystal structure

determination of a newly synthesized benzothiazole copper(II) complex, J. Mol. Struct. 1261 (2022) 132905. https://doi.org/10.1016/j.molstruc.2022.132905.

[35] A. Ali, M. Khalid, M. Ashfaq, A. N. Malik, M. N. Tahir, M. A. Assiri, M. Imran, S. F. d. AlcântaraMorais, A. A. C. Braga, Preparation, QTAIM and Single-Crystal Exploration of the Pyrimethamine-Based Co-Crystal Salts with Substituted Benzoic Acids, Organic & Supramolecular Chemistry. 7 (2022) e202200349. https://doi.org/10.1002/slct.202200349.

[36] S. S. Hasanova, L. N. Mamedova, M. Ashfaq, K. S. Munawar, E. M. Movsumov, M. Khalid, M. N. Tahir, M. Imran, Synthesis, crystal structure, Hirshfeld surface analysis and theoretical investigation of polynuclear coordination polymers of cobalt and manganese complexes with nitrobenzene and pyrazine, J. Mol. Struct. 1250 (2022) 131851 https://doi.org/10.1016/j.molstruc.2021.131851.

[37] A. M. Maharramov, G. S. Duruskari, G. Z. Mammadova, A. N. Khalilov, J. M. Aslanova, J. Cisterna, A. Cárdenas, I. Brito, A.M. Maharramov et al., crystal structure and hirshfeld surface analysis of (E)-5-phenyl-3-((4-(trifluoromethyl) benzylidene) amino) thiazolidin-2-iminium Bromide, J. Chil. Chem. Soc. 64 (2019) 4441–4447. http://dx.doi.org/10.4067/S0717-97072019000204441.

[38] G. Nandini, D.N. Sathyanarayana, Ab initio studies on molecular conformation and vibrational spectra of propionamide, J. Mol. Struct. THEOCHEM. 586 (2002) 125–135. https://doi.org/10.1016/S0166-1280(02)00079-9.

[39] Y. Kuroda, Y. Saito, K. Machida, T. Uno, Vibrational Spectra of propionamide and Its C-and N-Deuterated Compounds , Bull. Chem. Soc. Jpn. 45 (1972) 2371–2383. https://doi.org/10.1246/bcsj.45.2371.

[40] L. Yang, D.R. Powell, R.P. Houser, Structural variation in copper(i) complexes with

pyridylmethylamide ligands: Structural analysis with a new four-coordinate geometry index, τ_4, J. Chem. Soc. Dalt. Trans. (2007) 955–964. https://doi.org/10.1039/b617136b.

[41] M.S. Lassoued, M.S.M. Abdelbaky, W. Ben Soltan, A. Lassoued, S. Ammar, A. Gadri, A. Ben Salah, S. García-Granda, Structure characterization, photoluminescence and dielectric properties of a new hybrid compound containing chlorate anions of zincate (II), J. Mol. Struct. 1158 (2018) 221–228. https://doi.org/10.1016/j.molstruc.2018.01.027.

[42] S. Dgachi, M.M. Turnbull, F. Mezzadri, A.J. Norquist, A. Soran, J. Boonmak, G. Nemes, H. Naïli, Polymorphism in the metal–organic hybrid $(PhCH_2NEt_3)_2[CoBr_4]$: Synthesis, crystal structures and physico-chemical characterizations, Inorganica Chim. Acta. 514 (2021) 119997. https://doi.org/10.1016/j.ica.2020.119997.

[43] N. Amiri, S. Nouir, M. Hajji, T. Roisnel, T. Guerfel, G. Simonneaux, H. Nasri, Synthesis, structure, photophysical properties and biological activity of a cobalt(II) coordination complex with 4,4′-bipyridine and porphyrin chelating ligands, J. Saudi Chem. Soc. 23 (2019) 781–794. https://doi.org/10.1016/j.jscs.2019.03.003.

[44] K.L. Jyothi, R. Gautam, D. Swain, T.N. Guru Row, N.K. Lokanath, Cocrystals of Gallic Acid with Urea and Propionamide: Supramolecular Structures, Hirshfeld Surface Analysis, and DFT Studies, Cryst. Res. Technol. 54 (2019) 1–11. https://doi.org/10.1002/crat.201900016.

[45] M. Montazerozohori, A. Masoudiasl, S. Farokhiyani, S. Joohari, P. McArdle, Sonochemical synthesis of a new cobalt(II) complex: Crystal structure, thermal behavior, Hirshfeld surface analysis and its usage as precursor for preparation of CoO/Co_3O_4 nanoparticles, Ultrason. Sonochem. 38 (2017) 134–144. https://doi.org/10.1016/j.ultsonch.2017.03.017.

[46] A.A. Nejo, G.A. Kolawole, A.O. Nejo, Synthesis, characterization, antibacterial, and thermal studies of unsymmetrical Schiff-base complexes of cobalt(II), J. Coord. Chem. 63 (2010) 4398–4410. https://doi.org/10.1080/00958972.2010.532871.

[47] N. Mahfoudh, K. Karoui, M. Gargouri, A. BenRhaiem, Optical and electrical properties and conduction mechanism of $[(CH_3)_2NH_2]_2CoCl_4$, Appl. Organomet. Chem. 34 (2020) 1–12. https://doi.org/10.1002/aoc.5404.

[48] A. Tounsi, S. Elleuch, B. Hamdi, R. Zouari, A. Ben Salah, Structural study, Hirshfeld surface analysis, spectroscopic properties and DFT investigation of a new hybrid compound: $(C_6H_{10}(NH_3)_2)_3[CoCl_4](Cl)_4.3H_2O$, J. Mol. Struct. 1141 (2017) 512–523. https://doi.org/10.1016/j.molstruc.2017.04.003.

[49] H. Tllili, S. Walha, S. Elleuch, B. Fares Ali, H. Naïli, Structural, vibrational, DFT and optical studies of a new non-centrosymmetric hybrid material $(C_4H_{12}N_2)[CoBr_4]$, J. Mol. Struct. 1152 (2018) 303–310. https://doi.org/10.1016/j.molstruc.2017.09.096.

[50] J. Tauc, Optical Properties of Amorphous Semiconductors, Amorphous and Liquid Semiconductors. Springer US. (1974) 159-220. https://doi.org/10.1007/978-1-4615-8705-7_4

[51] P. Dhamodharan, K. Sathya, M. Dhandapani, Physico-chemical characterization, density functional theory (DFT) studies and Hirshfeld surface analysis of a new organic optical material: 1H-benzo[d]imidazol-3-ium-2,4,6-trinitrobenzene-1,3 bis(olate), J. Mol. Struct. 1146 (2017) 782–792. https://doi.org/10.1016/j.molstruc.2017.06.022.

[52] I. Dakhlaoui, K. Karoui, F. Hajlaoui, N. Audebrand, T. Roisnel, F. Jomni, $[(CH_3)_3N(CH_2)_2Br]_2[CoBr_4]$ halogenometallate complex: crystal structure, high-temperature reversible phase transition, electrical and optical properties, J. Mol. Struct. 1231 (2021) 129684. https://doi.org/10.1016/j.molstruc.2020.129684.

[53] A. El-Korashy, H. El-Zahed, M. Radwan, Optical studies of $[N(CH_3)_4]_2CoCl_4$, $[N(CH_3)_4]_2MnCl_4$ single crystals in the normal paraelectric phase, Phys. B Condens. Matter. 334 (2003) 75–81. https://doi.org/10.1016/S0921-4526(03)00019-X.

[54] A. Abkari, I. Chaabane, K. Guidara, Synthesis, crystal structure, spectroscopic characterization and optical properties of bis(4-acetylanilinium) tetrachlorocobalt (II), Phys. E Low-Dimensional Syst. Nanostructures. 86 (2017) 210–217. https://doi.org/10.1016/j.physe.2016.06.013.

[55] M. Abbassi, R. Ternane, I. Sobrados, A. Madani, M. Trabelsi-Ayadi, J. Sanz, Ionic conductivity of apatite-type solid electrolyte ceramics $Ca_{2-x}Ba_xLa_4Bi_4(SiO_4)_6O_2$ ($0 \leq x \leq 2$), Ceram. Int. 39 (2013) 9215–9221. https://doi.org/10.1016/j.ceramint.2013.05.026.

[56] A. Kumar, B.P. Singh, R.N.P. Choudhary, A.K. Thakur, Characterization of electrical properties of Pb-modified $BaSnO_3$ using impedance spectroscopy, Mater. Chem. Phys. 99 (2006) 150–159. https://doi.org/10.1016/j.matchemphys.2005.09.086.

[57] S. El Kossi, F.I.H. Rhouma, J. Dhahri, K. Khirouni, Structural and electric properties of $La_{0.7}Sr_{0.25}Na_{0.05}Mn_{0.9}Ti_{0.1}O_3$ ceramics, Phys. B Condens. Matter. 440 (2014) 118–123. https://doi.org/10.1016/j.physb.2014.01.016.

[58] M. Ram, Synthesis and electrical properties of $(LiCo_{3/5}Fe_{1/5}Mn_{1/5})VO_4$ ceramics, Solid State Sci. 12 (2010) 350–354. https://doi.org/10.1016/j.solidstatesciences.2009.11.012.

[59] S. Lanfredi, P.S. Saia, R. Lebullenger, A.C. Hernandes, Electric conductivity and relaxation in fluoride, fluorophosphate and phosphate glasses: Analysis by impedance spectroscopy, Solid State Ionics. 146 (2002) 329–339. https://doi.org/10.1016/S0167-2738(01)01030-X.

[60] N. Weslati, M. Ben Gzaiel, I. Chaabane, F. Hlel, Ionic conduction mechanism and relaxation studies of $NaNbAlP_3O_{12}$ compound, Ionics (Kiel). 24 (2018) 181–188. https://doi.org/10.1007/s11581-017-2170-2.

[61] S. Kulkarni, B.M. Nagabhushana, N. Parvatikar, A. Koppalkar, C. Shivakumara, R. Damle, Dielectric and electrical studies of Pr^{3+} doped nano $CaSiO_3$ perovskite ceramics, Mater. Res. Bull. 50 (2014) 197–202. https://doi.org/10.1016/j.materresbull.2013.10.029.

[62] F.S. Howell, R.A. Bose, P.B. Maado, C.T. Modynihan, Electrical Relaxation in a Glass-Forming Molten Salt , J. Phys. Chem. 78 (1974) 639–648. https://doi.org/10.1021/j100599a016.

[63] K.L. Gordon, J.H. Kang, C. Park, P.T. Lillehei, J.S. Harrison, A novel negative dielectric constant material based on phosphoric acid doped poly(benzimidazole), J. Appl. Polym. Sci. 125 (2012) 2977–2985. https://doi.org/10.1002/app.36248.

[64] S. Hajlaoui, I. Chaabane, A. Oueslati, K. Guidara, Anomalous dielectric behavior in centrosymmetric organic-inorganic hybrid bis-tetrapropylammonium hexachlorostannate. Crystal structure and properties, Solid State Sci. 25 (2013) 134–142. https://doi.org/10.1016/j.solidstatesciences.2013.09.004.

[65] A. Piecha, A. Gągor, M. Węcławik, R. Jakubas, W. Medycki, Anomalous dielectric behaviour in centrosymmetric organic-inorganic hybrid chlorobismuthate(III) containing functional N,N-dimethylethylammonium ligand. Crystal structure and properties, Mater. Res. Bull. 48 (2013) 151–157. https://doi.org/10.1016/j.materresbull.2012.10.018.

[66] S.A. Mansour, I.S. Yahia, F. Yakuphanoglu, The electrical conductivity and dielectric properties of C.I. Basic Violet 10, Dye. Pigment. 87 (2010) 144–148. https://doi.org/10.1016/j.dyepig.2010.03.011.

[67] M. Hamdi, S. Karoui, A. Oueslati, S. Kamoun, F. Hlel, Synthesis, crystal structure and dielectric properties of the new organic -inorganic hybrid compound $[C_6H_{10}N_2]_7[Bi_2Cl_{11}]_2{\cdot}4[Cl]$, J. Mol. Struct. 1154 (2018) 516–523. https://doi.org/10.1016/j.molstruc.2017.10.063.

TABLE CAPTIONS

Table 1. Crystallographic data and structure refinements of $[Co(PM)_6][CoBr_{1.93}Cl_{2.07}]$ complex.

Table S1. Fractional atomic coordinates and equivalent thermal factors (U_{eq}) or isotropic (U_{iso}) for $[Co(PM)_6][CoBr_{1.93}Cl_{2.07}]$.

Table S2. Anisotropic thermal stirring factors.

Table S3. Attribution of the different modes of vibration relative to $[Co(PM)_6][CoBr_{1.93}Cl_{2.07}]$ complex**.**

Table S4. Selected bond distances (Å) and angles (°) of $[Co(PM)_6][CoBr_{1.93}Cl_{2.07}]$.

Table 2. Hydrogen-bonding geometry of the title complex.

FIGURE CAPTIONS

Fig. S1. Scanning electron microscope analysis spectrum of $[Co(PM)_6][CoBr_{1.93}Cl_{2.07}]$.

Fig. S2. IR absorption spectrum of the title complex.

Fig. S3. The 3D representation of the Hirshfeld surface of (a) cationic part and (b) anionic, mapped with d_{norm} of $[Co(PM)_6][CoBr_{1.93}Cl_{2.07}]$.

Fig. S4. The 2D-fingerprint plots with the relative contributions of the different intermolecular contacts percentages to the hirshfeld surface area occurring in (a) $[Co_{1/2}(PM)_6]^{2+}$ cationic part and (b) $[Co(BrCl)_4]^{2-}$ anionic part of $[Co(PM)_6][CoBr_{1.93}Cl_{2.07}]$.

Fig. S5. Variation of the real part M' of the complex modulus as a function of the frequency at various temperatures.

Fig. S6. 3D presentation of the imaginary part of (M''/M''_{max}) versus frequency for different temperatures.

Fig. S7. Variation of (log (*f*p)) versus 1000/T of the $[Co(PM)_6][CoBr_{1.93}Cl_{2.07}]$ complex.

Fig. 1. Representation of the formula unit of $[Co(PM)_6][CoBr_{1.93}Cl_{2.07}]$ extended by symmetry to give complete octahedra around Co(II) cations (symmetry codes: (i) −*x*+2, −*y*+2, −*z*+1; (ii) −*x*+1, −*y*, −*z*+1).

Fig. 2. Packing of $[Co(PM)_6][CoBr_{1.93}Cl_{2.07}]$ along the crystallographic *c*-axis.

Fig. 3. Packing of $[Co(PM)_6][CoBr_{1.93}Cl_{2.07}]$ showing hydrogen bonds, are represented by dashed lines.

Fig. 4. (a) The TGA analysis curve (b) Differential scanning calorimetry measurements of $[Co(PM)_6][CoBr_{1.93}Cl_{2.07}]$.

Fig. 5. UV–Visible Absorption Spectra for the title complex.

Fig. 6. Variations of (a) $(\alpha h\nu)^{1/2}$ versus hν, (b) $(\alpha h\nu)^2$ versus hν at room temperature for $[Co(PM)_6][CoBr_{1.93}Cl_{2.07}]$.

Fig. 7. Variations of (αhν) versus Ln (hν - Eg) and the Energy diagram of $[Co(PM)_6][CoBr_{1.93}Cl_{2.07}]$ complex.

Fig. 8. Complex impedance and equivalent circuit of $[Co(PM)_6][CoBr_{1.93}Cl_{2.07}]$ complex shown for different temperatures.

Fig. 9. Frequency variation of (a) real part Z' and (b) imaginary part Z'' of the impedance at different temperatures for $[Co(PM)_6][CoBr_{1.93}Cl_{2.07}]$.

Fig. 10. Variation of (Ln (σ_{dc}T)) versus 1000/T of the $[Co(PM)_6][CoBr_{1.93}Cl_{2.07}]$ complex.

Fig. 11. Temperature dependence of (a) ε'_r and (b) ε''_r for $[Co(PM)_6][CoBr_{1.93}Cl_{2.07}]$ complex at various frequencies.

Graphical abstract